Self-Adaptive Physics-Informed Neural Networks for CO2 Immiscible Flooding in Low-Permeability Oil Reservoirs

Lyu, Xiaocong; Qin, Xue; Voskov, Denis; Liu, Huiqing; Wang, Jing

DOI
10.2118/223838-MS

Publication date
2025

Document Version
Final published version

Published in
Society of Petroleum Engineers - SPE Reservoir Simulation Conference, RSC 2025

SPE-223838-MS

Self-Adaptive Physics-Informed Neural Networks for CO2 Immiscible Flooding in Low-Permeability Oil Reservoirs

Xiaocong Lyu and Xue Qin, State Key Laboratory of Petroleum Resources and Prospecting, China University of Petroleum, Beijing, China; Denis Voskov, Department of Geoscience and Engineering, TU Delft, Delft, Netherlands / Department of Energy Science and Engineering, Stanford University, CA, USA; Huiqing Liu and Jing Wang, State Key Laboratory of Petroleum Resources and Prospecting, China University of Petroleum, Beijing, China

 DOI 10.2118/223838-MS

This paper was prepared for presentation at the SPE Reservoir Simulation Conference held in Galveston, Texas, USA, 25–27 March 2025.

Abstract

Physics-Informed Neural Networks (PINNs) gains attentions as a promising approach for applying deep neural networks to the numerical solution of nonlinear partial differential equations (PDEs). However, due to the challenging regions within the solutions of 'stiff' PDEs, e.g., shock front of CO_2 immiscible flooding, adaptive methods are essential to ensure the neural network accurately addresses these issues.

In this work, we introduce a novel method for adaptively training PINNs, named Self-Adaptive PINNs (SA-PINNs). This approach employs fully trainable adaptation weights that are applied individually to each training point. Consequently, the neural network autonomously identifies challenging regions of the solution space and focuses its learning efforts on these areas. This method is hereby used to simulate a two-phase immiscible flooding in a low-permeability oil reservoir, with considering gas dissolution and the threshold pressure gradient of oil phase in low-permeability oil reservoirs, i.e., modified Buckley-Leverett (B-L) problem.

The model is capable of generating a precise physical solution, accurately capturing both shock and rarefaction waves under the specified initial and boundary conditions, though the introduction of complicated physics increases the nonlinearity of the governing PDEs. The self-adaptive mechanism modifies the behavior of the deep neural network by simultaneously minimizing the losses and maximizing the weights. It, thus, can effectively capture the non-linear characteristics of the solution, thereby overcoming the existing limitations of PINNs. In these numerical experiments, the SA-PINNs demonstrated superior performance compared to other state-of-the-art PINN algorithms in terms of L2 error. Moreover, it was also achieved with a reduced number of training epochs.

SA-PINNs can effectively model the dynamics of complex physical systems by optimizing network parameters to minimize the residuals of the PDEs.

Keywords: Self-adaptive physics-informed neural networks, CO_2 Immiscible flooding, Low-Permeability oil reservoirs, Gas dissolution, Threshold pressure gradient

Introduction

Physics-informed neural networks (PINNs) represent a significant advancement in the field of numerical methods for solving partial differential equations (PDEs) (Raissi et al., 2019, Beck et al., 2020, Cai et al., 2021). Traditional approaches to solving PDEs, such as finite difference methods, finite volume methods, and finite element methods, rely heavily on discretizing the spatial and temporal domains and solving the resulting algebraic systems (Coats et al., 1995, Peaceman, 2000, Chen, 2007). While these methods are well-established and powerful, they can become computationally expensive and complex, particularly for high-dimensional problems or those involving complex geometries and boundary conditions (Chang and Yortsos, 1992, Li and Tchelepi, 2015). PINNs offer a promising alternative by leveraging the power of neural networks to approximate solutions to PDEs in a more flexible and potentially more efficient manner (Yu et al., 2022, Rodriguez-Torrado et al., 2022, McClenny and Braga-Neto, 2023).

At the core of PINNs is the idea of embedding the physical laws governing the system, expressed as PDEs, directly into the structure of the neural network (Mao et al., 2020, Cai et al., 2021, Xie et al., 2023). This is achieved by incorporating the PDEs into the loss function of the neural network. During training, the neural network learns not only from the data but also from the underlying physical laws (Pang et al., 2019). This means that the network is guided to find solutions that satisfy both the data and the PDE constraints. The result is a model that can generalize well to unseen data and accurately capture the dynamics of the physical system being studied (Raissi et al., 2019). The process of training a PINN involves defining a neural network architecture and a loss function that includes terms representing the PDE residuals, initial conditions, and boundary conditions (Cai et al., 2021, Jagtap et al., 2022). The PDE residuals are computed using automatic differentiation, a technique that allows the derivatives of the neural network outputs with respect to the inputs to be calculated efficiently. This enables the seamless integration of the PDE constraints into the learning process. By minimizing the loss function, the network adjusts its parameters to satisfy the PDEs as closely as possible, resulting in an approximate solution to the PDE.

PINNs represent a novel and powerful approach to solving PDEs, combining the strengths of neural networks with the rigor of physical laws. Their ability to handle high-dimensional problems, incorporate diverse data types, and solve both forward and inverse problems positions them as a transformative tool in many aspects. However, despite their promising potential, PINNs faces also some challenges (Fuks and Tchelepi, 2020, Cuomo et al., 2022, Shan et al., 2023). One significant issue is their sensitivity to hyperparameter selection. The performance of PINNs can vary greatly depending on the choice of learning rates, network architectures, and other training parameters (Chuang and Barba, 2023, Huang and Agarwal, 2023). This sensitivity often requires extensive trial and error, making the optimization process time-consuming and computationally expensive. In addition, PINNs struggle with complex or highly nonlinear PDEs. These types of equations often lead to convergence issues or require a significantly larger number of training epochs to achieve acceptable accuracy. Moreover, the imposition of boundary and initial conditions can be challenging. While PINNs incorporate these conditions into the loss function, ensuring that the network adequately satisfies these constraints can be difficult, especially for high-dimensional problems. This difficulty can result in suboptimal solutions that do not fully adhere to the physical constraints of the problem.

To address some of these limitations, self-adaptive physics-informed neural networks (SA-PINNs) have been developed. Due to its special structure, SA-PINNs can dynamically adjust hyperparameters during training (McClenny and Braga-Neto, 2023). By employing adaptive algorithms that can modify learning rates and other parameters on-the-fly, SA-PINNs reduce the need for extensive manual tuning and can more efficiently navigate the solution space. This adaptability not only speeds up the training process but also enhances the robustness and accuracy of the resulting solutions (Xiang et al., 2022, Saleh et al., 2024). Self-adaptive mechanisms can also help the network focus on challenging regions of the solution space, e.g., shock front in a two-phase displacement system, ensuring better convergence and adherence to physical

constraints (Guo et al., 2023). By automatically adjusting the weights assigned to different components of the loss function, SA-PINNs can more effectively balance the enforcement of boundary and initial conditions with the minimization of the residual of the PDE.

In this work, SA-PINNs are adopted to solve CO_2 immiscible flooding in a low-permeability reservoir, incorporating the complex phenomena of CO_2 dissolution and threshold pressure gradients in the modified Buckley-Leverett (BL) equations. These physical processes are highly nonlinear, which significantly challenges the conventional PINNs. By leveraging the adaptive capabilities of SA-PINNs, the model is able to dynamically adjust its parameters and improve accuracy in capturing the intricate behaviors of CO_2 phase interactions and flow characteristics within porous media, particularly for the shock front prediction. This approach provides a robust framework for addressing the nonlinearities inherent in CO_2 flooding processes, thereby offering significant advancements in predictive modeling for enhanced oil recovery and carbon sequestration strategies.

Methodology

Governing equations

In this work, we consider the CO_2 injection to enhance the oil recovery process, i.e., two-phase, two-component incompressible transport for miscible and immiscible flooding. The mass-conservation equations for CO_2 and oil components are expressed as:

$$\frac{\partial}{\partial t}\left(\phi\sum_{j=1}^{np}x_{cj}\rho_j S_j\right)+\mathrm{div}\sum_{j=1}^{np}\left(x_{cj}\rho_j u_j\right)+\sum_{j=1}^{np}x_{cj}\rho_j\widetilde{q}_j=0,\qquad c=1,2,\cdots,n_c \tag{1}$$

where ϕ is porosity, and x_{cj} is the mole fraction of component c in phase j. ρ_j and S_j are the phase molar density and saturation. u_j and $\widetilde{q_j}$ are phase velocity and phase rate per unit volume.

For simplification, we assume that the pressure and temperature are constant. In addition, the phase molar density is equal and constant, i.e., gas saturation (S_g) is equal to gas molar fraction (V). Then Eq. 1 be rewritten as:

$$\phi\frac{\partial\left(x_{co}(1-V)+y_{cg}V\right)}{\partial t}+\frac{\partial\left(x_{co}u_o+y_{cg}u_g\right)}{\partial t}=0,\quad c=1,2. \tag{2}$$

Without the effects of buoyancy and capillary forces, the phase velocity of one-dimensional (1D) flow based on Darcy's law is expressed as:

$$u_j=-\frac{KK_{rj}}{\mu_j}\frac{dp}{dx},\qquad j=\mathrm{oil},\ \mathrm{gas}, \tag{3}$$

where K is the formation absolute permeability, μ_j and K_{rj} are phase viscosity and relative permeability, respectively.

Summing Eqs. 3 for all phases yields the total velocity:

$$u_t=u_g+u_o=-K\left(\frac{K_{ro}}{\mu_o}+\frac{K_{rg}}{\mu_g}\right)\frac{dp}{dx}. \tag{4}$$

For 1D incompressible flow, assuming that u_t is constant (i.e., the injection rate is fixed), the transport equation becomes:

$$\begin{cases}\phi\frac{\partial z_c}{\partial t}+u_t\frac{\partial F_c}{\partial x}=0, & C=1,2,\\ F_c=y_{cg}f_g+x_{co}\left(1-f_g\right), & C=1,2,\\ z_c=y_{cg}V+x_{co}(1-V), & C=1,2,\end{cases} \tag{5}$$

where z_c is the overall composition of component c and F_c is the fractional flow of the component c. f_g is the dimensionless gas flux function, referred to as the gas fractional flow, which is defined as:

$$f_g = \frac{\mathbf{u_g}}{\mathbf{u_t}} = \frac{\frac{\mathrm{Krg}}{\mu_g}}{\frac{\mathrm{Kro}}{\mu_o} + \frac{\mathrm{Krg}}{\mu_g}}. \tag{6}$$

For the immiscible two-phase B-L transport test case, the fractional flow F_c is equivalent to f_g.

In the immiscible case, due to the consideration of CO_2 dissolution in oil, the conventional B-L equation is modified to a concentration balance equation, without the effects of phase compressibility and gravity segregation. Then the front velocity of CO_2 can be expressed in fractional flow:

$$\begin{cases} \frac{\partial C_{co_2}}{\partial T_D} + \frac{\partial F_{co_2}}{\partial x_D} = 0, \\ C_{co_2} = S_g C_{co_2,g} + S_o C_{co_2,o}, \\ F_{co_2} = f_g C_{co_2,g} + \left(1 - f_g\right) C_{co_2,o}, \end{cases} \tag{7}$$

where T_D and x_D are dimensionless time and dimensionless distance, which are expressed as $\frac{qB_g t}{\phi AL}$ and $\frac{x}{L}$, respectively. C_{CO_2} is the total concentration of CO_2 in gas and oil phase, and F_{CO_2} is the CO_2 fractional flow. $C_{CO_2,o}$ and $C_{CO_2,g}$ are CO_2 concentration in gas and oil phase, respectively.

The concentration of CO_2 in the oil and gas phases can be expressed by the solubility:

$$\begin{cases} C_{CO_2,o} = \frac{R_{so}}{22.4\left(R_{so}B_g + 1\right)}, \\ C_{CO_2,g} = \frac{1}{22.4B_g}, \end{cases} \tag{8}$$

where R_{so} and B_g are the dissolved gas/oil ratio and gas volume factor, respectively.

Self-adaptive physics-informed neural networks

Physics-Informed Neural Networks (PINNs) represent an innovative approach that integrates physics-based modeling with the powerful approximation capabilities of neural networks. The core idea behind PINNs is to embed the governing physical laws, often represented as partial differential equations (PDEs), directly into the loss function of the neural network. Let $u(x,t)$ represent the solution to a physical problem governed Eq. 1 or Eq. 2:

$$\mathrm{N}(\mathrm{u}(\mathrm{x}, \mathrm{t}); \lambda) = 0, \ \mathrm{x} \in \Omega, \ \mathrm{t} \in [0, \mathrm{T}], \tag{9}$$

where N is a differential operator parameterized by λ, x denotes the spatial coordinates, and t represents time. The goal of PINNs is to approximate the solution $u(x,t)$ using a neural network $\hat{u}(x, t; \theta)$ with parameters θ.

This loss function typically consists of two components: data loss and physics loss. Data loss ensures that the network's predictions are consistent with any available observational or experimental data. If u_{data} represents the observed data at specific points $(x_i, t_i)_{i=1}^{N}$, the data loss can be expressed as:

$$L_{data}(\theta) = \frac{1}{N}\sum_{i=1}^{N} \left|\hat{u}(x_i, t_i; \theta) - u_{data}(x_i, t_i)\right|^2, \tag{10}$$

Physics loss enforces the satisfaction of the governing PDEs by penalizing the deviation of the network's output from the differential operator N :

$$L_{physics}(\theta) = \frac{1}{M}\sum_{i=1}^{M} \left|N(\hat{u}(x_i, t_i; \theta); \lambda)\right|^2, \tag{11}$$

where M is the number of collocation points selected within the domain Ω.

The overall loss function is then a weighted sum of the data loss and the physics loss:

$$L(\theta) = \alpha L_{data}(\theta) + \beta L_{physics}(\theta), \tag{12}$$

where α and β are weighting factors that balance the contributions of the data and physics terms. By minimizing this combined loss function through gradient-based optimization, the network parameters θ are adjusted so that the neural network solution $\hat{u}(x_i, t_i; \theta)$ not only fits the data but also satisfies the underlying physical laws.

A unique feature of SA-PINNs is their self-adaptive mechanism, which dynamically adjusts the weights of different loss components during training (Fig. 1). This adaptive weighting allows the network to focus more on difficult regions of the solution space, improving convergence and accuracy. Specifically, the total loss L_{total} is given by:

$$L_{total} = \xi_1(t) MSE_{\mathcal{L}_{B\&I}} + \xi_2(t) MSE_{\mathcal{L}_{PDE}} \ , \tag{13}$$

where $\xi_1(t)$ and $\xi_2(t)$ are time-dependent weighting functions. These functions are designed to increase the emphasis on the most difficult regions of the solution space or the most violated conditions, ensuring that the network allocates more resources to areas that require greater precision.

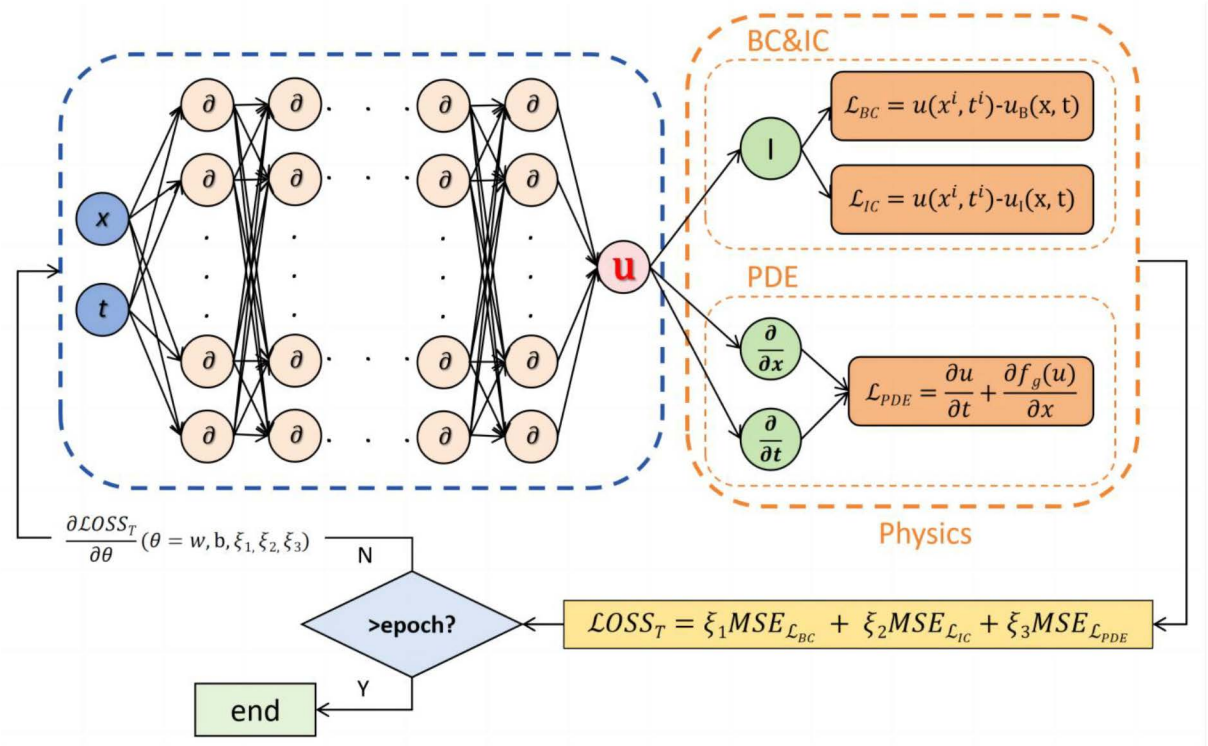

Figure 1—The diagram of the PINN model framework employed in this study is here. The MLP network comprises 7 hidden layers, each containing 20 neurons. The network features two inputs and one output (predicting the gas saturation,S_g). The term 'epoch' denotes the number of update iterations.

The self-adaptive mechanism can be mathematically formulated as:

$$\xi_1(t) = \frac{exp(\lambda_a L_{B\&I}(t))}{\sum_j exp(\lambda_j L_j(t))}, \tag{14}$$

$$\xi_2(t) = \frac{exp(\lambda_\beta L_{PDE}(t))}{\sum_j exp(\lambda_j L_j(t))}, \tag{15}$$

where λ_a and λ_β are hyperparameters that control the sensitivity of the weights to the corresponding loss components.

During training, the neural network adjusts its parameters θ to minimize the total loss L_{total}. The adaptive weights ensure that the network focuses more on the regions where the residuals are largest, thereby improving the accuracy of the solution in those regions. The training process can be formulated as:

$$\theta^* = \arg\min_\theta L_{total}(\theta). \tag{16}$$

By dynamically adjusting the weights, SA-PINNs can effectively handle the complexities of multi-scale and highly heterogeneous problems, which are often challenging for traditional PINNs. This self-adaptive mechanism makes SA-PINNs particularly suitable for solving PDEs with localized features or sharp gradients, where uniform training can lead to suboptimal solutions.

Numerical examples

In this work, we investigate the performance of the SA-PINNs on CO_2 flooding with both immiscible and compositional scenarios. The parameters used are listed in Table 1. The relative permeability model and viscosity model are shown in Appendix A and Appendix B.

Tab 1—Fluid properties and initial/boundary conditions used in this work.

Cases	μ_g,cp	$\mu_{(o,i)}$,cp	S_{gr}	S_{or}	n_g	K_{rge}	K_{roe}	Initial condition	Boundary conditions
Immiscible	0.05	5	0.05	0.1	4	1	1	$S_g = S_{gr}$	$S_g = 1 - S_{or} - S_{gr}$
Compositional			0.05	0.1				$z_{CO2} = 0$	$z_{CO2} = 1$

The performance of the SA-PINNs on CO_2 immiscible flooding is presented. The main figure of merit used is the L2-error:

$$L_2 = \frac{\sqrt{\sum_{i=1}^{N_U} |u(x_i, t_i) - U(x_i, t_i)|^2}}{\sqrt{\sum_{i=1}^{N_U} |U(x_i, t_i)|^2}}, \tag{17}$$

where $u(x,t)$ is the training approximation, and $U(x,t)$ is a high-fidelity solution over a fine mesh x_i,t_i with N_U points.

Results and discussions

CO_2 immiscible flooding with dissolution

Fig. 2 illustrates the evolution of gas saturation profiles (S_g) over dimensionless distance (x_D) at various time steps (t) for three different approaches. At the early time steps (e.g., t=0.05, 0.15, 0.25), all three methods exhibit a sharp front in the gas saturation distribution, characteristic of the Buckley-Leverett solution. The SA-PINNs method shows remarkable consistency with the exact solution, particularly in maintaining the sharpness of the shock front, capturing the transition between the gas-invaded and non-invaded regions with high accuracy. On the other hand, the conventional PINNs slightly underestimate the steepness of the shock front and show small deviations from the exact solution, especially near the gas saturation front. As the displacement process evolves at later time steps (t=0.60, 0.90), these differences become more pronounced.

The exact solution continues to show a sharp saturation front, while the SA-PINNs closely follows the exact solution in both the location and shape of the front, adapting effectively as the front propagates further into the medium. Conventional PINNs, however, display more significant deviations in capturing the sharp discontinuities, where the gas saturation front becomes more diffuse in the PINNs results compared to both the exact solution and SA-PINNs. These observations suggest that the SA-PINNs method, with its adaptive nature, offers superior performance in handling the steep saturation gradients and complex front dynamics characteristic of the Buckley-Leverett problem, while the conventional PINNs struggle to maintain accuracy as the displacement front moves deeper into the domain.

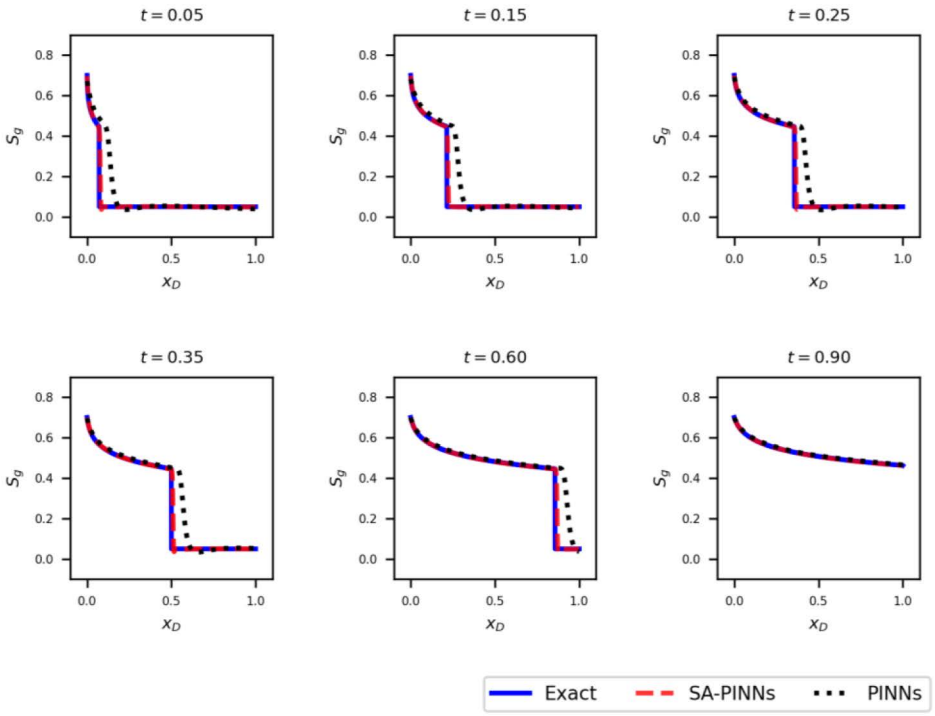

Figure 2—Variations of gas saturation with x_D at different times. The solid blue line is the exact solution from the BL equation. The dashed red and black lines are predicted data from SA-PINNs and PINNs, respectively.

Fig. 3 shows a visual comparison between the true data, predicted data, and the absolute error for gas saturation obtained at different times. Fig. 3(a) shows the true data from the BL equation, while Fig. 3(b) depicts the predicted data from the SA-PINNs model. Both figures exhibit a similar color distribution, indicating that the SA-PINNs model successfully captures the gas saturation behavior over time, as the saturation increases from the lower left to the upper right. The similarity in the color gradient across both figures suggests that the SA-PINNs provide an accurate approximation of the true solution. Fig. 3(c) presents the absolute error between the true and predicted data, illustrating the magnitude of the discrepancies between the two datasets. The error is concentrated along the diagonal line, which corresponds to the location of the sharp saturation front in the Buckley-Leverett solution. Despite this, t he overall error remains small, with most of the domain showing minimal deviations, as represented by the blue color. The relatively low error, particularly away from the shock front, demonstrates the capability of SA-PINNs to accurately capture the overall gas saturation dynamics while maintaining a high degree of precision across the spatial and temporal domains. This confirms that SA-PINNs can effectively model gas saturation in multiphase flow problems while minimizing prediction errors.

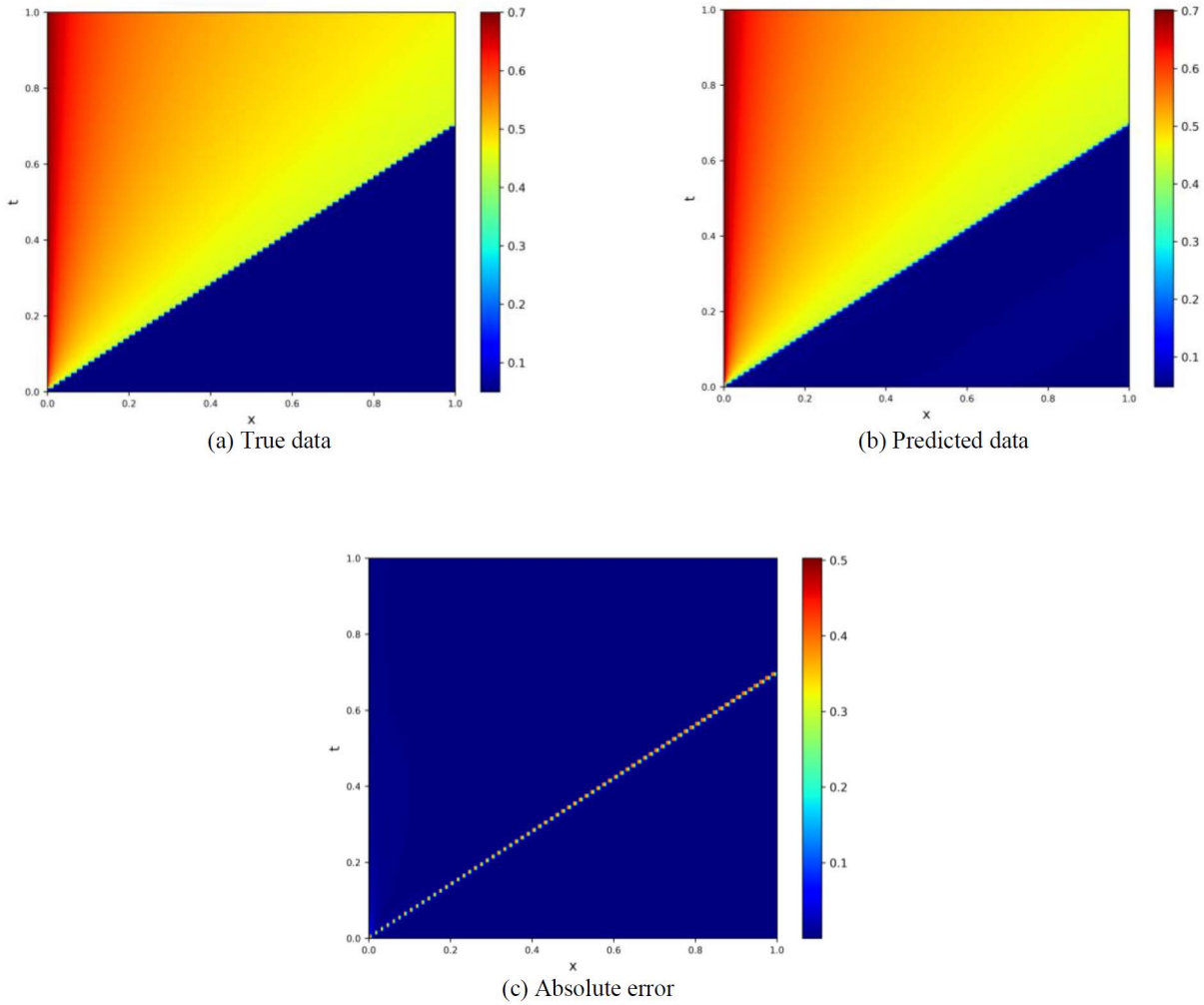

Figure 3—Gas saturation and absolute error distribution at different times and locations. Absolute error is the difference between true data and predicted data obtained from SA-PINNs.

Fig. 4 shows the loss values for the training of conventional PINNs and SA-PINNs over 20000 epochs. The loss components are broken down into total loss, initial condition loss, boundary condition loss, and PDE loss for both methods. For the conventional PINNs, the total loss, boundary, and PDE loss gradually decrease, but there are significant fluctuations, particularly in the PDE loss, which suggests difficulties in learning the physical dynamics accurately. Moreover, while the initial condition loss decreases significantly, it stabilizes at a higher value compared to SA-PINNs, indicating that the conventional PINNs struggle to fit the initial conditions as well as SA-PINNs. The SA-PINNs show a much smoother convergence for all components, with a significantly lower overall loss after 20000 epochs. Notably, the initial condition loss drops by several orders of magnitude, and the PDE loss is much lower and more stable compared to conventional PINNs. This suggests that SA-PINNs handle the learning process more efficiently, particularly by better adapting to the solution of the PDE and fitting the initial and boundary conditions.

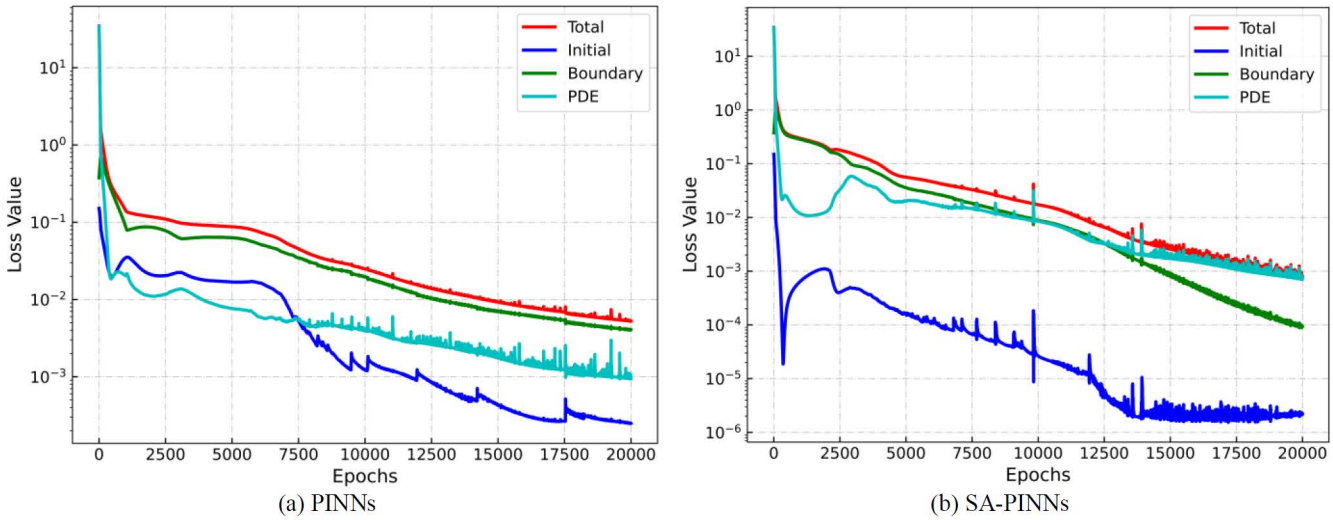

Figure 4—Variations of loss values with the number of update iterations. The loss functions include the total loss and each part in the PDE, i.e., initial, boundary, and PDE.

Fig. 5 compares the R^2 values, which quantify the accuracy of the model's predictions relative to the true data, over dimensionless time (t_D) for conventional PINNs and SA-PINNs. The results show that SA-PINNs consistently outperform conventional PINNs across the entire time range. Initially, both models start with lower R^2 values due to the challenge of fitting the sharp initial conditions, but SA-PINNs quickly approach near-perfect accuracy, stabilizing at R^2 values close to 1 after $t_D = 0.2$. Conventional PINNs, while following a similar trend, exhibit a notable dip in performance around t_D =0.65, where the R^2 value temporarily drops before the gas breakthrough. This suggests that PINNs struggle to capture the solution accurately at breakthrough time, possibly due to difficulties in resolving complex dynamics, i.e., abrupt changes of front. In contrast, SA-PINNs maintain higher accuracy and stability throughout the entire simulation, indicating their superior ability to adapt to and model the dynamic evolution of gas saturation over time. This highlights the improved robustness and reliability of SA-PINNs, especially when handling challenging regions in the solution space.

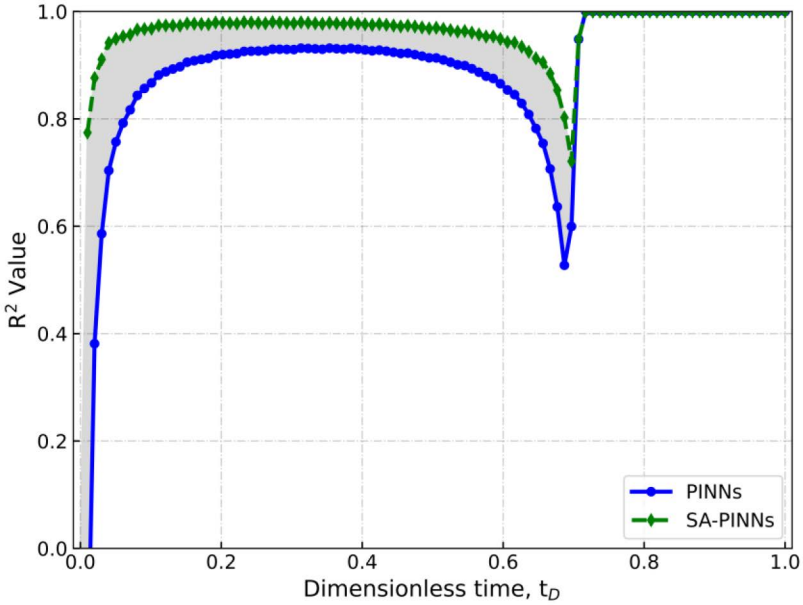

Figure 5—Comparison of R^2 values over t_D for conventional PINNs and SA-PINNs.

CO_2 compositional flooding

Fig. 6 shows the CO_2 mole fraction distribution over dimensionless distance at various time steps. At early time steps (t=0.05,0.10,0.15), the trailing shock is well-defined in all results. Both PINNs and SA-PINNs accurately capture the steep gradient of the trailing shock, closely following the analytical solution from the BL equation. For the leading shock, the differences between the methods are more pronounced. The exact solution shows a clear leading shock with a rapid transition in the mole fraction, while both SA-PINNs and conventional PINNs exhibit some difficulties in accurately predicting the position and sharpness of this shock. The leading shock in the SA-PINNs is closer to the exact solution, but some discrepancies are still evident, particularly in the transition region between the high and low CO_2 mole fraction values. The conventional PINNs, on the other hand, show significant deviations from the exact solution, with a smoother and less distinct leading shock.

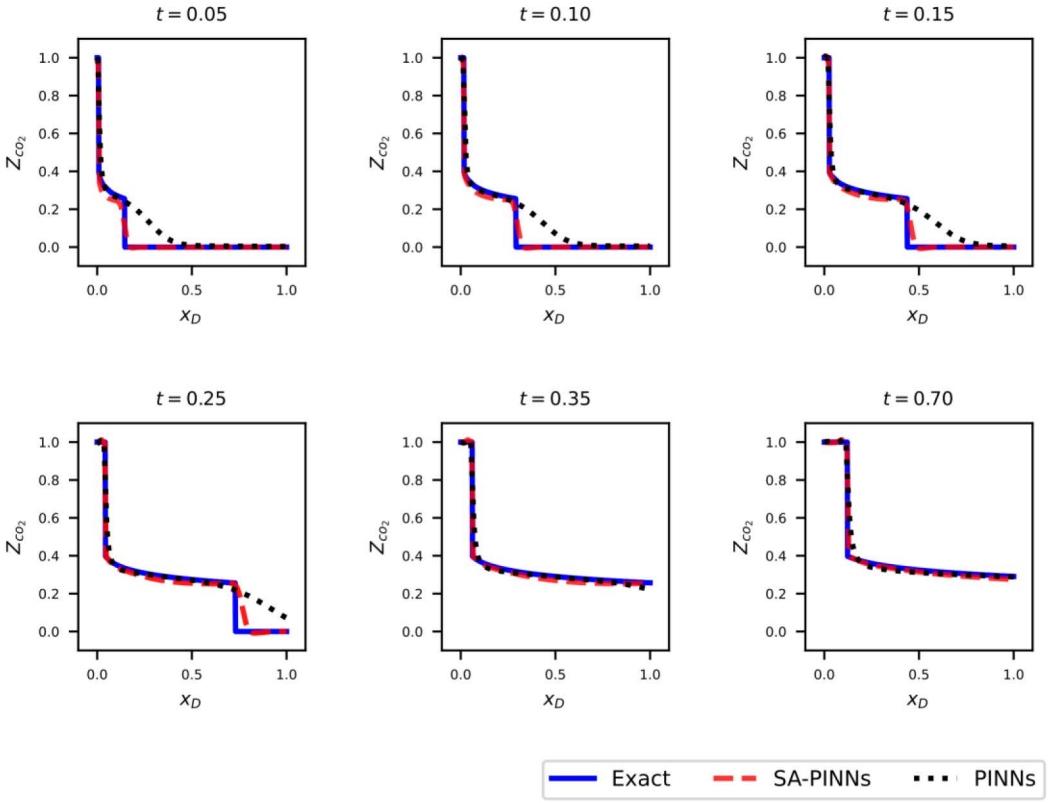

Figure 6—Variations of CO_2 mole fraction with x_D at different times. The solid blue line is the exact solution from the BL equation. The dashed red and black lines are predicted data from SA-PINNs and PINNs, respectively.

As time progresses, the leading shock continues to propagate forward until CO_2 breaks through, and the SA-PINNs maintain their accuracy in tracking this shock. By t=0.35 and t=0.70, the SA-PINNs almost perfectly capture the leading shock, matching the exact solution's sharpness and position. The conventional PINNs, while improving, still lag behind in accurately capturing the full sharpness of the leading shock, particularly at t=0.25. However, by t=0.70, the conventional PINNs improve significantly and follow the exact solution more closely, though some diffusion in the shock front remains. For the trailing shock, both methods improve over time, but the SA-PINNs remain superior in capturing the characteristics. The conventional PINNs still show some diffusion at later times, indicating persistent difficulties in resolving the trailing shock as effectively as SA-PINNs. By t=0.70, the trailing shock predicted by SA-PINNs is almost indistinguishable from the exact solution, while the conventional PINNs exhibit a smoother transition, lacking the distinct sharpness seen in the exact solution. This smoothing effect indicates that conventional PINNs struggle to resolve the steep gradient at the shock front.

Fig. 7 illustrates the comparison between true data and predicted data from SA-PINNs for the CO_2 mole fraction at different times. Fig. 7(a) shows the true CO_2 mole fraction distribution, while Fig. 7(b) presents the predicted mole fraction using SA-PINNs. It demonstrates that SA-PINNs are able to accurately reproduce the CO_2 mole fraction distribution over time, with very similar patterns in both spatial and temporal directions. Fig. 7(c) shows the absolute error between the two datasets over time and space. It reveals that most of the errors are concentrated along the transition front, where the CO_2 mole fraction experiences sharp changes. This is expected due to the complexity of capturing the steep gradients at the shock fronts, which are typical in displacement problems. Despite these localized errors, the overall error values are small, indicating that SA-PINNs are highly effective in predicting the CO_2 mole fraction with minimal deviation from the true BL solution.

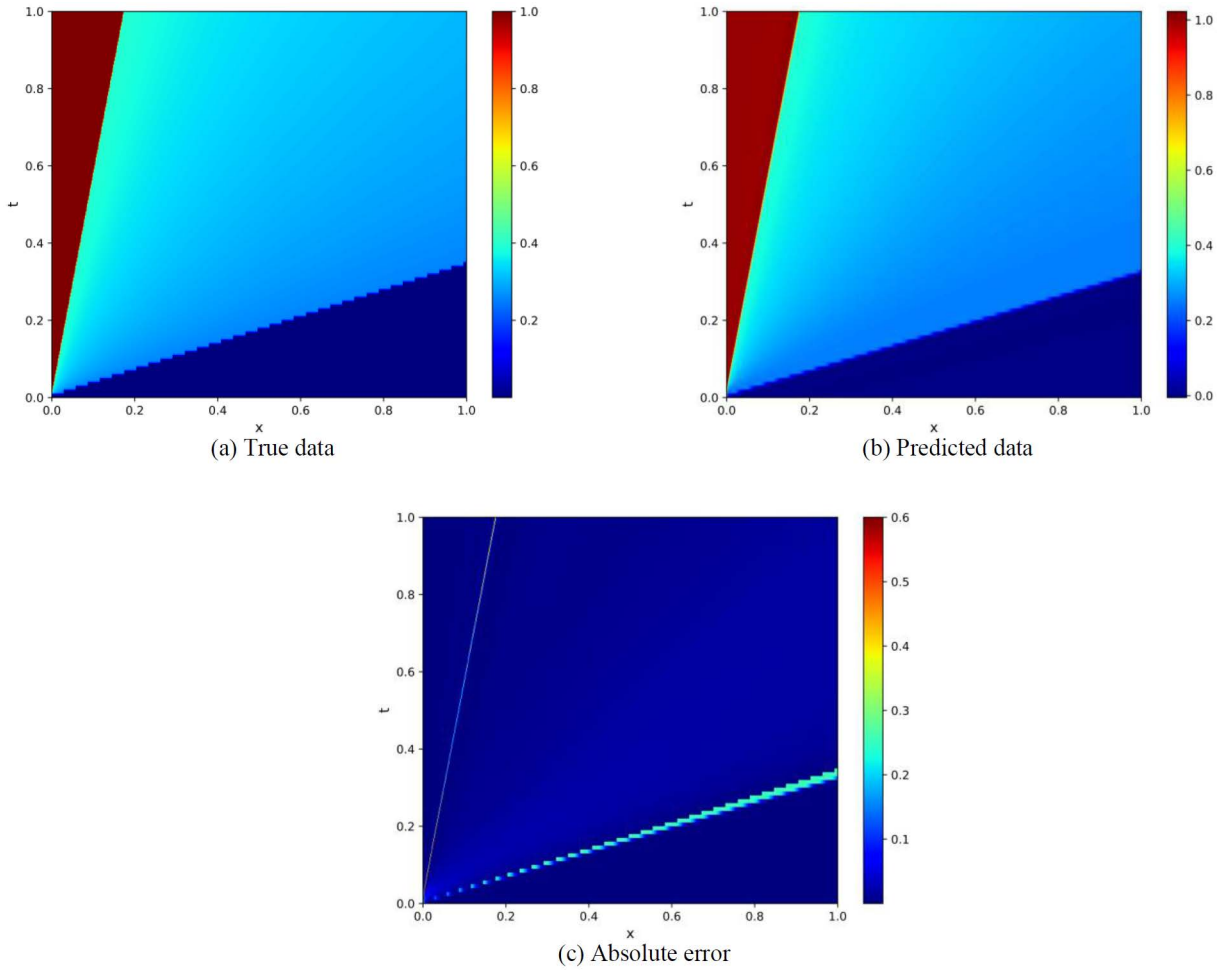

Figure 7—CO_2 mole fraction and absolute error distribution at different times and locations. Absolute error is the difference between true data and predicted data obtained from SA-PINNs.

Fig. 8 presents the comparison of loss values between conventional PINNs and SA-PINNs over the course of 20,000 epochs. In the conventional PINNs (Fig. 8(a), while the total loss steadily decreases over time, there are noticeable inefficiencies in how the initial condition, boundary condition, and PDE losses evolve. The initial condition loss starts high but plateaus at a relatively slower rate, stabilizing only after a significant number of epochs. Similarly, the PDE loss decreases but remains several orders of magnitude higher than desired, showing fluctuations as training progresses. The boundary condition loss in conventional PINNs is particularly unstable, exhibiting significant oscillations even in the later stages of training, suggesting that the model struggles to maintain accuracy in enforcing boundary conditions.

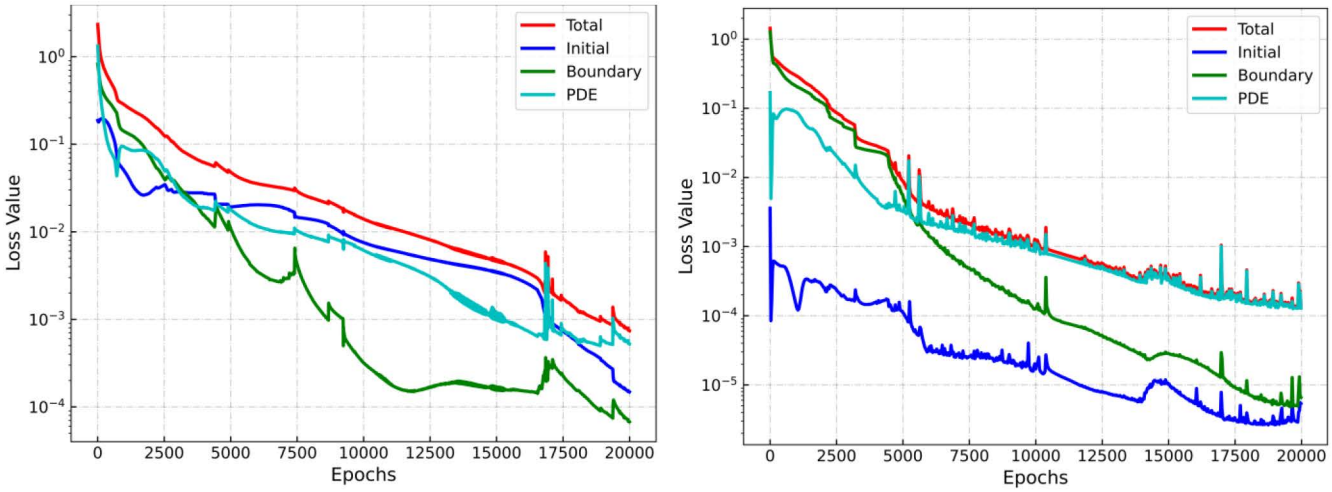

Figure 8—Variations of loss values with the number of update iterations in the CO_2 miscible flooding. The loss functions include the total loss and each part in the PDE, i.e., initial, boundary, and PDE.

By comparison, the SA-PINNs (Fig. 8(b)) demonstrate a much smoother and more efficient convergence. The total loss, as well as each individual loss component, declines more quickly, with the initial condition and boundary condition losses reaching much lower values than in the conventional PINNs. The PDE loss is also minimized far more effectively, stabilizing at lower values without the erratic fluctuations observed in the conventional PINNs. The overall training behavior of SA-PINNs is much more stable, indicating that the self-adaptive approach allows the model to balance the competing loss components more effectively. The SA-PINNs also exhibit fewer issues with boundary conditions, as indicated by the smoother boundary loss curve, allowing for more accurate modeling of physical processes governed by partial differential equations.

Fig. 9 illustrates the R^2 values over dimensionless time (t_D) for PINNs and SA-PINNs in CO_2 miscible flooding. The SA-PINNs consistently achieve higher R^2 values across the entire time domain compared to conventional PINNs, indicating superior predictive performance. Both methods exhibit an initial rise in accuracy, with the SA-PINNs reaching near-perfect accuracy ($R^2 \approx 1.0$) by$t_D \approx 0.2$, while the PINNs lag slightly behind, stabilizing at lower R^2 values. There is a noticeable drop in performance for both models around t_D =0.6, where the R^2 value briefly decreases, likely due to challenges in accurately capturing complex shock dynamics at the time when the leading shock breaks through. However, SA-PINNs recover quickly, maintaining higher accuracy through the remainder of the time domain. This suggests that SA-PINNs not only provide more accurate predictions but also adapt more effectively to the complexities of the physical problem, particularly when dealing with sharp fronts or transitions in the CO_2 mole fraction distribution.

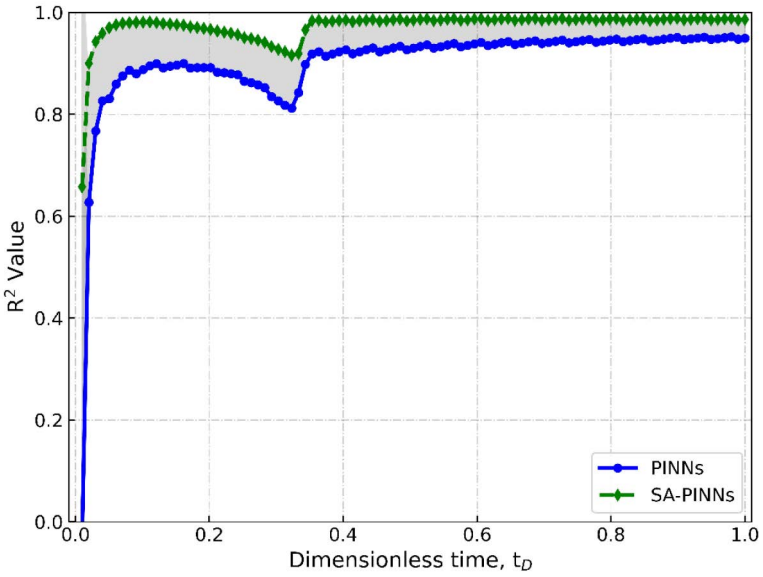

Figure 9—Comparison of R^2 values over t_D for conventional PINNs and SA-PINNs in the case of CO_2 miscible flooding.

Conclusions

Based on the results presented, several key conclusions can be drawn regarding the performance of self-adaptive physics-informed neural networks (SA-PINNs) compared to conventional physics-informed neural networks (PINNs):

SA-PINNs consistently demonstrate higher accuracy in predicting gas saturation and CO_2 mole fraction distributions, as evidenced by the higher R^2 values and smaller absolute errors in the results. The SA-PINNs achieve near-perfect accuracy much earlier in the dimensionless time, indicating superior convergence and predictive capability.

Both leading and trailing shock fronts in the displacement process are more accurately captured by SA-PINNs compared to conventional PINNs. While conventional PINNs struggle with smoothing effects and errors near sharp transitions, SA-PINNs effectively resolve these complex dynamics, particularly as the saturation and CO_2 fronts propagate through the system.

The loss values from SA-PINNs are significantly lower and exhibit more stable convergence compared to conventional PINNs. This is particularly evident in the initial condition, boundary condition, and PDE loss components, where SA-PINNs show faster and more reliable reductions.

SA-PINNs provide more robust performance over a wide range of time steps, recovering quickly from challenging regions (e.g., around t_D =0.6) where conventional PINNs show greater performance degradation. The adaptive mechanism in SA-PINNs allows for more efficient training, better generalization, and more accurate long-term predictions.

Acknowledgements

We acknowledge the National Natural Science Foundation of China (No.52304054) and National Natural Science Foundation of China Joint Fund Project (No. U24B6003).

References

M. Raissi, P. Perdikaris, G. E. Karniadakis, Physics-informed neural networks: A deep learning framework for solving forward and inverse problems involving nonlinear partial differential equations. *Journal of Computational physics* **378**(2019), 686–707. https://doi.org/10.1016/j.jcp.2018.10.045.

C. Beck, M. Hutzenthaler, A. Jentzen, B. Kuckuck, An overview on deep learning-based approximation methods for partial differential equations, arXiv preprint arXiv:2012.12348 (2020). https://doi.org/10.48550/arXiv.2012.12348.

S. Cai, Z. Wang, S. Wang, P. Perdikaris, G. E. Karniadakis, Physics-informed neural networks for heat transfer problems. *Journal of Heat Transfer* **143** (2021) 060801. https://doi.org/10.1115/1.4050542.

K. H. Coats, K. Coats, L. Thomas, R. Pierson, Compositional and black oil reservoir simulation, in: *SPE Reservoir Simulation Conference*, SPE, 1995, pp. SPE–29111. https://doi.org/10.2118/29111-MS.

Peaceman D. W., Fundamentals of numerical reservoir simulation, Elsevier, 2000.

Chen Z., Reservoir simulation: mathematical techniques in oil recovery, *SIAM*, 2007.250. https://doi.org/10.1111/j.1468-8123.2008.00220.x.

J. Chang, Y. C. Yortsos, Effect of capillary heterogeneity on buckley-leverett displacement, SPE reservoir engineering 7 (1992) 285–293. https://doi.org/10.2118/18798-PA.

B. Li, H. A. Tchelepi, Nonlinear analysis of multiphase transport in porous media in the presence of viscous, buoyancy, and capillary forces, *Journal of Computational Physics* **297** (2015) 104–131. https://doi.org/10.1016/j.jcp.2015.04.057.

J. Yu, L. Lu, X. Meng, G. E. Karniadakis, Gradient-enhanced physics-informed neural networks for forward and inverse pde problems, *Computer Methods in Applied Mechanics and Engineering* **393** (2022) 114823. https://doi.org/10.1016/j.cma.2022.114823.

R. Rodriguez-Torrado, P. Ruiz, L. Cueto-Felgueroso, M. C. Green, T. Friesen, S. Matringe, J. Togelius, Physics-informed attention-based neural network for hyperbolic partial differential equations: application to the buckley–leverett problem, *Scientific reports 12* (2022) 7557. https://doi.org/10.48550/arXiv.2105.07898.

L. D. McClenny, U. M. Braga-Neto, Self-adaptive physics-informed neural networks, *Journal of Computational Physics* **474** (2023) 111722. https://doi.org/10.1016/j.jcp.2022.111722.

Z. Mao, A. D. Jagtap, G. E. Karniadakis, Physics-informed neural networks for high-speed flows, *Computer Methods in Applied Mechanics and Engineering* **360** (2020) 112789. https://doi.org/10.1016/j.cma.2019.112789.

S. Cai, Z. Mao, Z. Wang, M. Yin, G. E. Karniadakis, Physics-informed neural networks (pinns) for fluid mechanics: A review, *Acta Mechanica Sinica* **37** (2021) 1727–1738. https://doi.org/10.48550/arXiv.2105.09506.

C. Xie, S. Du, J. Wang, J. Lao, H. Song, Intelligent modeling with physics-informed machine learning for petroleum engineering problems., *Advances in Geo-Energy Research* **8** (2023). https://doi.org/10.46690/ager.2023.05.01.

G. Pang, L. Lu, G. E. Karniadakis, fpinns: Fractional physics-informed neural networks, *SIAM Journal on Scientific Computing* **41** (2019) A2603–A2626. https://doi.org/10.1137/18M1229845.

A. D. Jagtap, Z. Mao, N. Adams, G. E. Karniadakis, Physics-informed neural networks for inverse problems in supersonic flows, *Journal of Computational Physics* **466** (2022) 111402. https://doi.org/10.1016/j.jcp.2022.111402.

O. Fuks, H. A. Tchelepi, Limitations of physics informed machine learning for nonlinear two-phase transport in porous media, *Journal of Machine Learning for Modeling and Computing* **1**(1) (2020). https://10.1615/JMachLearnModelComput.2020033905.

S. Cuomo, V. S. Di Cola, F. Giampaolo, G. Rozza, M. Raissi, F. Piccialli, Scientific machine learning through physics–informed neural networks: Where we are and what's next, *Journal of Scientific Computing* **92** (2022) 88. https://doi.org/10.48550/arXiv.2201.05624.

L. Shan, C. Liu, Y. Liu, Y. Tu, L. Dong, X. Hei, Physics-informed machine learning for solving partial differential equations in porous media., *Advances in Geo-Energy Research* **8** (2023). https://doi.org/10.46690/ager.2023.04.04.

P.-Y. Chuang, L. A. Barba, Predictive limitations of physics-informed neural networks in vortex shedding, arXiv preprint arXiv:2306.00230 (2023). https://doi.org/10.48550/arXiv.2306.00230.

A. J. Huang, S. Agarwal, On the limitations of physics-informed deep learning: Illustrations using first order hyperbolic conservation law-based traffic flow models, *IEEE Open Journal of Intelligent Transportation Systems* (2023). https://doi.org/10.48550/arXiv.2302.12337.

Z. Xiang, W. Peng, X. Liu, W. Yao, Self-adaptive loss balanced physics-informed neural networks, *Neurocomputing 496* (2022) 11–34. https://doi.org/10.1016/j.neucom.2022.05.015.

Saleh, A. N. Alquennah, A. Ghrayeb, S. S. Refaat, H. Abu-Rub, S. P. Khatri, A self-adaptive physics-informed gated recurrent unit neural networks model for estimating the lifetime of li-ion batteries, *Authorea Preprints* (2024). https://api.semanticscholar.org/CorpusID:270355539.

Y. Guo, X. Cao, K. Peng, Solving nonlinear soliton equations using improved physics-informed neural networks with adaptive mechanisms, *Communications in Theoretical Physics* **75** (2023) 095003. https://10.1088/1572-9494/accb8d.

Corey A. T., The interrelation between gas and oil relative permeabilities, Producers monthly 19 (1954) 38–41. https://cir.nii.ac.jp/crid/1570009749409873792.

R. Wang, C. Lv, S. Zhao, Z. Lun, H. Wang, M. Cui, Experiments on three-phase relative permeability in CO2 flooding for low permeability reservoirs, in: *SPE Asia Pacific Enhanced Oil Recovery Conference*, SPE, 2015, p. D011S001R005. https://doi.org/10.2118/174590-MS.

Appendix A

Relative-permeability model

The relative-permeability model implemented here is the classical Brooks-Corey model(Corey, 1954), where the phase relative permeability only depends on its own saturation:

$$K_{ro} = \left(\frac{S_o - S_{org}}{1 - S_{wc} - S_{org}} \right)^{n_o}, \quad \text{(Appendix A.1)}$$

$$K_{rg} = \left(\frac{S_g - S_{gc}}{1 - S_{wc} - S_{gc}} \right)^{ng}, \quad \text{(Appendix A.2)}$$

where, S_{wc}, S_{org}, and S_{gc} are the residual water saturation, residual oil saturation, and residual gas saturation, respectively. K_{roe} and K_{rge} are the oil end-point relative permeability and gas end-point relative permeability. n_g and n_o are the gas and oil relative permeability exponent, respectively. The interaction between CO_2 and oil leads to a complicated flow behavior in the low-permeability reservoirs. In this work, an improved relative-permeability model is implemented to represent the correlation between the Corey exponent n_o and reservoir pressure,

$$n_{rog} = \begin{cases} 1, & \left(p \geq p_{mmp}\right) \\ \frac{2p + p_{nm} + 3p_{mmp}}{p_{nm} - p_{mmp}} & \left(p_{mmp} > p > p_{nm}\right) \\ 3, & \left(p = p_{nm}\right) \end{cases} \quad \text{(Appendix A.3)}$$

where, p is the average reservoir pressure or injection pressure during displacement, and p_{mmp} is CO_2 - oil minimum miscibile pressure (MMP). P_{nm} is immiscible boundary pressure, usually associated with CO_2 - oil interfacial tension being greater than or equal to 7 mN/m.

Appendix B

Modified oil-viscosity model

For immiscible flooding, the solubility of CO_2 in oil increases with pressure. Based on the experimental data from (Wang et al., 2015), a linear relationship between CO_2 solubility and pressure can be obtained:

$$R_{so} = 8.204p + 12.567, \quad \text{(Appendix B.1)}$$

Where R_{so} is the solubility of CO_2 in oil.

The dissolution of CO_2 into the oil phase causes the volume of oil to expand and further reduces oil viscosity. To describe the viscosity reduction effect owing to CO_2 dissolution, the modified oil viscosity can be expressed,

$$\begin{cases} \ln\mu_o = X_o ln\mu_{oi} + X_g ln\mu_g \\ \alpha = 0.255\gamma_o - 4.16T_r^{1.85}\frac{e^{7.36} - e^{7.36(1-p_r)}}{e^{7.36}-1} \\ T_r = \frac{1.8T+32}{547.57} \\ X_g = \frac{V_g}{\alpha V_o + V_g} \\ V_g = \frac{R_{so}B_g}{1+R_{so}B_g} \\ p_r = 0.1354p \\ B_g = \frac{p_s z T}{p T_s} \\ V_o = 1 - V_g \\ X_o = 1 - X_g \\ Z = 1 - \frac{3.25p}{10^{0.9813T_r}} + \frac{0.274p_r^2}{10^{0.9813T_r}} \end{cases} \quad \text{(Appendix B.2)}$$

where μ_o is the viscosity of oil after CO_2 dissolution, μ_{oi} is the initial oil viscosity, μ_g is the viscosity of CO_2, V_g and V_o is the volume fractions of CO_2 and oil after CO_2 dissolution, B_g is volume coefficient of CO_2. According to the method of Papay, z is the compressibility factor of CO_2. And T is the reservoir temperature, p_s and T_s is the pressure and the temperature at standard conditions, γ_o is the relative density of oil, T_r and p_r is the relative temperature and pressure.

For the miscible case, we still use the correlation in Eq. Appendix B.2 to calculate the mixture viscosity. Instead of using CO_2 solubility, the equation of state (EOS) is implemented to evaluate the interactions between CO_2 and oil. With the assumption of local equilibrium, the multi-phase system should satisfy:

$$Z_c - \sum_{j=1}^{np} v_j x_{cj} = 0, \quad \text{(Appendix B.3)}$$

$$f_c^g(p, T, x_g) - f_c^w(p, T, x_w) = 0, \quad \text{(Appendix B.4)}$$

$$\sum_{c=1}^{n_c} (x_{cg} - x_{cw}) = 0, \quad \text{(Appendix B.5)}$$

$$\sum_{j=1}^{np} v_j - 1 = 0. \quad \text{(Appendix B.6)}$$

Here $Z_c = \sum_j x_{cj}\rho_j s_j / \sum_j \rho_j s_j$ is overall molar composition of component c and f_{cj} (p, T, x_j) is the fugacity of component C in phase j. v_j is phase j molar fraction.